Faraday pilot-wave dynamics: modelling and computation

Paul A. Milewski[1,†], **Carlos A. Galeano-Rios**[2], **André Nachbin**[2] and **John W. M. Bush**[3]

[1]Department of Mathematical Sciences, University of Bath, Bath BA2 7AY, UK

[2]IMPA/National Institute of Pure and Applied Mathematics, Est. D. Castorina, 110, Rio de Janeiro, RJ 22460-320, Brazil

[3]Department of Mathematics, MIT, Cambridge, MA, USA

A millimetric droplet bouncing on the surface of a vibrating fluid bath can self-propel by virtue of a resonant interaction with its own wave field. This system represents the first known example of a pilot-wave system of the form envisaged by Louis de Broglie in his double-solution pilot-wave theory. We here develop a fluid model of pilot-wave hydrodynamics by coupling recent models of the droplet's bouncing dynamics with a more realistic model of weakly viscous quasi-potential wave generation and evolution. The resulting model is the first to capture a number of features reported in experiment, including the rapid transient wave generated during impact, the Doppler effect and walker–walker interactions.

Key words: capillary waves, drops, Faraday waves

1. Introduction

Louis de Broglie ([1926](#), [1930](#), [1987](#)) proposed that microscopic particles such as electrons move in resonance with a guiding wave field centred on the particle and generated by its internal vibration. The resulting pilot-wave theory represented the first example of what are now widely known as hidden-variable theories, attempts to underpin the statistical theory of quantum mechanics with a rational dynamics. While de Broglie's pilot-wave theory was successful in rationalizing single-particle diffraction, on the basis of which he won the Nobel prize in 1929, his theory was superseded by the Copenhagen Interpretation, despite its inherent philosophical vagaries (Bacchiagaluppi & Valentini [2009](#)). At the time that de Broglie proposed his pilot-wave theory of quantum dynamics, there was no macroscopic analogue to draw from. A hydrodynamic pilot-wave system was discovered a decade ago by Yves Couder and Emmanuel Fort (Couder *et al.* [2005*b*](#); Protière, Boudaoud & Couder [2006](#); Eddi *et al.* [2011](#)), and takes the form of millimetric fluid droplets walking on the surface of a vibrating fluid bath. The relation between this system and the modern extensions of de Broglie's mechanics has recently been explored by Bush ([2015](#)).

† Email address for correspondence: p.a.milewski@bath.ac.uk

By virtue of its accompanying wave field, the walking droplet, or 'walker', is a spatially extended object, and exhibits several features previously thought to be exclusive to the microscopic quantum realm (Bush 2010). Central to the walker dynamics is the concept of path memory (Eddi *et al.* 2011): the wave force imparted to the walker depends on the pilot-wave field generated by its previous bounces. The more long-lived its waves, the longer its path memory. The walker dynamics is thus explicitly non-local in time: prediction of the walker's future requires knowledge not only of its present state, but also of its past.

Eddi *et al.* (2009*b*) demonstrated that the walkers can tunnel across submerged barriers in a manner reminiscent of quantum tunnelling. Fort *et al.* (2010) demonstrated the emergence of orbital quantization for droplets walking in a rotating frame, and developed the dynamic analogy with Landau orbits. Most strikingly, this hydrodynamic pilot-wave system has been shown to exhibit wave-like statistics in three separate geometries. Couder & Fort (2006) examined the diffraction of walkers through single- and double-slit geometries, and demonstrated a statistical behaviour reminiscent of that of single-particle diffraction of electrons and photons (Bach *et al.* 2013). Harris *et al.* (2013) examined a walker in a confined geometry, and demonstrated that the probability distribution function corresponds to the amplitude of the cavity's Faraday wave mode, a result reminiscent of electrons in a quantum corral (Crommie, Lutz & Eigler 1993*a,b*). Harris & Bush (2014) and Oza *et al.* (2014*a,b*) re-examined walkers in a rotating frame, and demonstrated that, at the highest forcing examined, the orbital quantization gives way to chaotic dynamics with wave-like statistics that emerge as the walker drifts between its unstable quantized eigenstates. Similar behaviour has been reported for walkers subjected to a central force (Perrard *et al.* 2014): the chaotic dynamics emerging in the limit of high vibrational forcing is characterized by the walker switching between unstable orbital states quantized in energy and angular momentum. Labousse *et al.* (2014) rationalize this behaviour through consideration of the energy landscape associated with the walker's wave field.

When a horizontal fluid layer is subject to a sinusoidal vertical vibration with frequency ω_0, its free surface becomes unstable to a standing field of Faraday waves when the acceleration amplitude Γ exceeds the Faraday threshold, Γ_F. These waves have half the frequency of the imposed vibration and a wavelength prescribed by the standard water-wave dispersion relation (Benjamin & Ursell 1954). Below the Faraday threshold, millimetric droplets may bounce on the bath surface provided an air layer is sustained between drop and bath during impact (Walker 1978). Below a critical bouncing threshold, the drops will merge with the underlying bath; above it, they will bounce indefinitely (Couder *et al.* 2005*a*). Just above the bouncing threshold, the drops bounce with the forcing frequency; however, as the forcing amplitude is increased progressively, the bouncing amplitude increases until eventually the bouncing period matches that of the subharmonic Faraday wave field. Resonance is thus achieved between the bouncing droplet and its accompanying wave field, energy is most readily transferred between the two, and one can view the bath as being a damped oscillator forced at resonance. In certain parameter regimes, these resonant bouncers are destabilized by their wave field, and give way to a regular walking state (Couder *et al.* 2005*b*; Protière *et al.* 2006). The walking drop lands just off-centre of the descending central peak of its wave field, thus acquiring at each impact a horizontal impulse that propels it forward. A millimetric drop may thus walk steadily across the surface of a vibrating fluid bath by virtue of a resonant interaction with its locally excited Faraday wave field.

Protière *et al.* (2005, 2006) and Eddi *et al.* (2008) presented a series of regime diagrams indicating the observed dependence of the droplet behaviour on the forcing acceleration and drop size. Moláček & Bush (2013*a*) pointed out that, for a given fluid, there are two principal control parameters that prescribe the dynamical behaviour of the system. The first, Γ/Γ_F, is a parameter indicating the distance from the Faraday threshold Γ_F. The second, the vibration number,

$$\Omega = \omega_0 \sqrt{\rho R_0^3/\sigma}, \tag{1.1}$$

indicates the relative magnitude of the imposed vibrational frequency ω_0 and the natural frequency of the drop of radius R_0, density ρ and surface tension σ. Moláček & Bush (2013*a*,*b*) developed a detailed description of the dynamics accompanying droplet impact. To leading order, the droplet deformation may be neglected, and the role of the interface may be treated as that of a linear spring with a spring constant proportional to the surface tension (Gilet & Bush 2009*a*,*b*). Through building on a model of quasi-static droplet impact on a rigid superhydrophobic surface Moláček & Bush (2012, 2013*a*) developed a model that incorporates the influence of droplet deformation and the inertia of the underlying fluid. The interface may then be described in terms of a logarithmic spring whose stiffness increases with depth of penetration. While the relatively low-energy bouncing states can be rationalized without considering the influence of the wave field generated by previous impacts, such is not the case for the walking threshold, which depends critically on the destabilizing influence of the wave field. The theoretical developments of Moláček & Bush (2013*a*,*b*) have now rationalized the regime diagrams describing the behaviour of bouncing drops (Protière *et al.* 2006; Eddi *et al.* 2008; Wind-Willassen *et al.* 2013). Detailed regime diagrams indicating the behaviour of the droplets in the Ω–Γ/Γ_F plane were presented in Moláček & Bush (2013*a*,*b*) and Wind-Willassen *et al.* (2013), who adopted the nomenclature defined in Gilet & Bush (2009*a*,*b*). A periodic bouncing state is denoted by $(m, n)^p$ if it bounces n times in m forcing periods. The superscript p represents an ordering of the modes with the same periodicity according to mean mechanical energy, with the highest p denoting the most energetic mode.

In addition to underscoring the importance of the vertical dynamics on the walking, the theoretical developments of Moláček & Bush (2013*a*,*b*) have yielded a trajectory equation (Oza, Rosales & Bush 2013) that has formed the basis of further theoretical developments, such as the model to be developed herein. In a certain parameter regime delineated and rationalized in Moláček & Bush (2013*b*) and Wind-Willassen *et al.* (2013), the walking drops achieve perfect resonance with their Faraday wave field: the combined impact time and time of flight is precisely equal to the Faraday period, $2/\omega_0$. Such resonant walkers are described in terms of the pilot-wave theory of Oza *et al.* (2013), who explicitly assume the resonance between walker and wave. Doing so allows them to recast the trajectory equation of Moláček & Bush (2013*b*) into an integro-differential form that is amenable to analysis. The resulting 'stroboscopic formulation' allowed for an accurate assessment of the stability of various simple forms of motion, including straight-line walking (Oza *et al.* 2013) as well as orbital motion both in a rotating frame (Harris & Bush 2014; Oza *et al.* 2014*a*) and in the presence of a central force (Perrard *et al.* 2014). It also captures much of the rich nonlinear behaviour arising in the high-memory limit, for example, the complex orbits arising in a rotating frame (Oza *et al.* 2014*b*).

In the wave models of Eddi *et al.* (2011), Moláček & Bush (2012) and Oza *et al.* (2013), the wave field created by each impact is described in terms of a standing

Bessel function $J_0(k_F r)$ centred on the point of impact, and damped in time at a rate prescribed by the system memory, which depends on both the proximity to the Faraday threshold and the fluid viscosity. This approximation is adequate to describe a droplet interacting with its own wave field in an unbounded fluid domain, where the short-time ($t \ll T_F$, where T_F is the forcing period) behaviour of the wave field is irrelevant, and the influence of reflections off the boundaries is not considered. However, it explicitly neglects the influence of the transient field generated by the impact, which travels at approximately 10 times the walker speed (Eddi *et al.* 2011) and may play a significant role in the interaction of multiple walkers, or the interaction of single walkers with topography or boundaries. As such effects are central to the storyline of the walking drops arising in bouncing lattices of walkers (Eddi *et al.* 2009*a*), tunnelling (Eddi *et al.* 2009*b*), motion in confined geometries (Harris *et al.* 2013) and single-particle diffraction (Couder & Fort 2006), we develop here a more sophisticated model of the wave field accompanying walkers that explicitly captures several time-dependent wave features generated by each impact.

Our goal is to develop a hydrodynamic pilot-wave model, formulated from first principles, that exhibits the behaviour observed in the laboratory experiments. In describing the wave field, our approach is inspired by the potential flow description of Benjamin & Ursell (1954), with viscous damping being incorporated in the manner outlined by Lamb (1932) and Dias, Dyachenko & Zakharov (2008) and recently analysed by Ambrose, Bona & Nicholls (2012). In §2, we formulate this model, which allows for the self-consistent generation and propagation of a Faraday pilot-wave field. In §3, we present our model results, demonstrating that our system exhibits a number of features of the walking droplets that have not been captured by previous models.

2. Formulation

We proceed by presenting a linear water-wave model with viscous damping, along the lines developed by Lamb (1932) and Dias *et al.* (2008). We then briefly review the Faraday instability problem and conclude with a coupled model whereby Faraday waves are generated by a localized time-dependent surface pressure forcing that models the impacting droplet.

2.1. *Governing equations*

In modelling the wave field generated by the bouncing droplet, we consider the three-dimensional free-surface water-wave problem with the following assumptions. We treat the fluid as being of infinite depth, an approximation valid for depths greater than half a wavelength, as is typically the case in the experiments of interest. We assume that viscous dissipation is non-negligible, and explicitly consider both gravitational and surface tension forces. We incorporate the vertical vibration of the bath in terms of a time-dependent gravitational force. Finally, we model the effect of droplet impact in terms of a time-dependent localized pressure applied at the free surface. With these assumptions, and letting (x, y) denote the horizontal plane and z the vertical direction, the fluid motion is governed by the incompressible Navier–Stokes equations:

$$\boldsymbol{u}_t + \boldsymbol{u} \cdot \nabla \boldsymbol{u} = -\frac{1}{\rho} \nabla p + \nu \Delta \boldsymbol{u} + \boldsymbol{F}(t), \quad z \leqslant \eta(x, y, t), \tag{2.1}$$

$$\nabla \cdot \boldsymbol{u} = 0, \quad z \leqslant \eta(x, y, t), \tag{2.2}$$

where the force due to gravity and the vertical shaking of the fluid is expressed $\boldsymbol{F} = (0, 0, -g + g\Gamma\cos(\omega_0 t))$. These equations must be solved subject to the appropriate boundary conditions. The condition of no motion at large depths requires that

$$\boldsymbol{u} \to 0 \quad \text{as } z \to -\infty. \tag{2.3}$$

At the free surface, the stress balance and the kinematic condition require, respectively, that

$$p\boldsymbol{n} - \rho\nu\boldsymbol{\tau} \cdot \boldsymbol{n} = (\sigma\kappa + P_D(x, y, t))\boldsymbol{n}, \quad z = \eta(x, y, t), \tag{2.4}$$

$$\eta_t + \boldsymbol{u} \cdot \nabla(\eta - z) = 0, \quad z = \eta(x, y, t). \tag{2.5}$$

Here $\boldsymbol{u} = (u, v, w)$ and p are the velocity and pressure fields, ρ is the fluid density and ν is the kinematic viscosity. For simplicity we have assumed a laterally unbounded domain, although we remark on boundary effects in the discussion of the Faraday problem below. The free-surface displacement is given by η, σ is the surface tension, $\kappa = \nabla \cdot \boldsymbol{n}$ is the free-surface curvature and $\boldsymbol{n}$ is the outward unit normal. The strain tensor $\boldsymbol{\tau}$ is given by $(\nabla\boldsymbol{u} + \nabla\boldsymbol{u}^{\mathrm{T}})$; and P_D is the pressure exerted by the droplet as it impinges on the free surface.

Two approximations are now made. First, as the observed wave slope is small, we linearize the equations. Second, following the approach of Dias *et al.* (2008) developed originally in Lamb (1932), we derive a 'weakly dissipative' surface-wave model. Specifically, we assume that the waves may be described to leading order as irrotational and inviscid, but that they also have a small rotational component resulting from the vanishing tangential stress-free surface boundary condition.

Neglecting, for the time being, the externally applied pressure from the droplet, we non-dimensionalize the system using the wave period T and wavelength λ. The result is

$$\boldsymbol{u}_t = -\nabla p + \epsilon\Delta\boldsymbol{u}, \quad z \leqslant 0, \tag{2.6}$$

$$\nabla \cdot \boldsymbol{u} = 0, \quad z \leqslant 0, \tag{2.7}$$

$$\boldsymbol{u} \to 0, \quad \text{as } z \to -\infty, \tag{2.8}$$

$$(p - G\eta + Bo\Delta_H\eta)\boldsymbol{n} = \epsilon\boldsymbol{\tau} \cdot \boldsymbol{n}, \quad z = 0, \tag{2.9}$$

$$\eta_t = w, \quad z = 0, \tag{2.10}$$

where having absorbed $\boldsymbol{F}$ into p it now denotes the dynamic pressure. Three non-dimensional parameters have been introduced: a reciprocal Reynolds number $\epsilon = \nu T/\lambda^2$, a Bond number $Bo = \sigma T^2/\rho\lambda^3$ and $G = gT^2/\lambda$; and Δ_H denotes the horizontal Laplacian. For the current experiments, characteristic values of the non-dimensional parameters, based on the physical constants listed in appendix B, $T = 1/40$ s and $\lambda = 0.5$ cm (corresponding to the most unstable Faraday wavelength) are $\epsilon = 0.02$, $Bo = 0.20$ and $G = 1.23$.

The small-viscosity dissipation model is obtained by introducing the Helmholtz decomposition of the velocity field

$$\boldsymbol{u} \equiv \nabla\phi + \epsilon\nabla \times \boldsymbol{\Psi}, \tag{2.11}$$

where ϕ results in a potential flow component, and $\boldsymbol{\Psi} = (\psi_1, \psi_2, \psi_3)$ in a vortical component. Specifically, the vortical components of the velocity field are $(\hat{u}, \hat{v}, \hat{w}) =$

$\nabla \times \boldsymbol{\Psi} = (\psi_{3,y} - \psi_{2,z}, \psi_{3,x} - \psi_{1,z}, \psi_{2,x} - \psi_{1,y})$. Substitution into the system (2.6)–(2.10) leads to the following set of equations, valid in the fluid bulk:

$$\phi_t + p = 0, \quad z \leqslant 0, \tag{2.12}$$

$$\Delta \phi = 0, \quad z \leqslant 0, \tag{2.13}$$

$$\psi_{j,t} = \epsilon \Delta \psi_j, \quad j = 1, 2, 3, \quad z \leqslant 0, \tag{2.14}$$

$$\phi, \psi_j \to 0 \quad \text{as } z \to -\infty. \tag{2.15}$$

The stress balance equations at $z = 0$ couple the potential and vortical velocity fields. The normal balance yields

$$(p - G\eta + Bo \Delta_H \eta) = 2\epsilon(\phi_z + \epsilon(\psi_{2,x} - \psi_{1,y}))_z, \tag{2.16}$$

while the tangential stress balances yield

$$0 = 2\phi_{xz} + \epsilon(\psi_{3,y} - \psi_{2,z})_z + \epsilon(\psi_{2,x} - \psi_{1,y})_x, \tag{2.17}$$

$$0 = 2\phi_{yz} + \epsilon(\psi_{1,z} - \psi_{3,x})_z + \epsilon(\psi_{2,x} - \psi_{1,y})_y. \tag{2.18}$$

Lastly, the kinematic condition is

$$\eta_t = \phi_z + \epsilon(\psi_{2,x} - \psi_{1,y}). \tag{2.19}$$

These equations are now simplified by using the boundary layer scaling $\partial_z = O(\epsilon^{-1/2})$ in $\boldsymbol{\Psi}$ and discarding higher-order terms. Then, we eliminate $\boldsymbol{\Psi}$ in favour of ϕ and η.

Truncating (2.16) at order ϵ and using (2.12) and (2.13), we obtain the final form of the dynamic boundary condition

$$\phi_t = G\eta - Bo \Delta_H \eta + 2\epsilon \Delta_H \phi. \tag{2.20}$$

The terms neglected are of order $\epsilon^{3/2}$. The tangential stress balance is now used to replace the viscosity-induced vertical velocity in the kinematic boundary condition. First, we use the boundary layer scaling to eliminate negligible contributions from the vortical flow and so arrive at the approximation

$$2\phi_{zx} = \psi_{2,zz} = \psi_{2,t}, \tag{2.21}$$

$$2\phi_{zy} = -\psi_{1,zz} = -\psi_{1,t}, \tag{2.22}$$

where (2.14) was used in the second equality. Now, use the leading-order term of the kinematic condition $\eta_t = \phi_z + O(\epsilon)$ to express ψ_1 and ψ_2 in terms of η:

$$\psi_2 = 2\eta_x + O(\epsilon), \tag{2.23}$$

$$\psi_1 = -2\eta_y + O(\epsilon). \tag{2.24}$$

Substituting into (2.19) yields the 'damped' kinematic condition

$$\eta_t = \phi_z + 2\epsilon \Delta_H \eta. \tag{2.25}$$

Again, terms of order $\epsilon^{3/2}$ arising from the horizontal stress balance were neglected. The damping term is merely the result of accounting for the leading-order term of the vertical component of vortical velocity at the free surface. Equations (2.20) and (2.25) were also presented in Dias *et al.* (2008), but there were obtained through arguments involving expanding the damped dispersion relation for the waves with $2\nu k^2/|\omega|$ as the small parameter. An analysis of the well-posedness of this formulation was recently given in Ambrose *et al.* (2012).

2.2. *Faraday waves*

When a vessel containing liquid is vibrated vertically, wave patterns will develop provided the Faraday threshold, Γ_F, is exceeded. Both the Faraday threshold and the form of the waves at the onset of instability will in general depend on both the fluid properties and the shape of the container. The first mathematical modelling of this Faraday instability was presented in Benjamin & Ursell (1954), who considered an inviscid fluid in a container of arbitrary cross-section. The influence of viscosity was elucidated by Kumar & Tuckerman (1994) and Kumar (1996), who demonstrate that, for a given configuration, the thresholds of the various modes of vibration depend explicitly on the fluid viscosity. We proceed by sketching how the stability analysis can be carried out with the equations derived above, through inclusion of weak viscous effects, in the case of an unbounded domain. Our first objective is to find the forcing threshold at which the planar free surface becomes unstable in our model. We note that all of the bouncing droplet phenomena of interest occur below this threshold, and depend on the proximity to the Faraday threshold (Eddi *et al.* 2011).

Based on the developments of the previous section, we formulate the problem as

$$\Delta\phi = 0, \quad z \leqslant 0, \tag{2.26}$$

$$\phi_t = g(1 - \Gamma\cos(\omega_0 t))\eta - \frac{\sigma}{\rho}\Delta_H\eta + 2\nu\Delta_H\phi, \quad z = 0, \tag{2.27}$$

$$\eta_t = \phi_z + 2\nu\Delta_H\eta, \quad z = 0, \tag{2.28}$$

together with $\nabla\phi \to 0$ as $z \to -\infty$. For a container of arbitrary cross-section, and in the inviscid limit ($\nu = 0$), one needs to satisfy $\phi_n = 0$ on the lateral walls of the container. Hence in the inviscid case, one chooses (Benjamin & Ursell 1954) $\phi = a_m(t)\Phi_m(x, y)e^{k_m z}$ and $k_m > 0$, with eigenfunctions Φ_m satisfying

$$-\Delta_H\Phi_m = k_m^2\Phi_m, \quad \frac{\partial\Phi_m}{\partial n} = 0 \quad \text{on } S, \tag{2.29a,b}$$

where S is the horizontal shape of the container, i.e. the curve corresponding to the intersection of the container boundaries with a horizontal plane. The amplitude equations for the eigenfunction coefficients a_m can then be shown to satisfy the Mathieu equations

$$\frac{d^2 a_m}{dt^2} + (\omega_m^2 - \omega_g^2\Gamma\cos(\omega_0 t))a_m = 0, \tag{2.30}$$

$$\omega_m^2 = \omega^2(k_m) = gk_m\left(1 + \frac{\sigma}{\rho g}k_m^2\right), \quad \omega_g^2 = gk_m. \tag{2.31}$$

When $\Gamma = 0$, there are only free oscillations of the liquid surface. Their frequency is given by the classical dispersion relation $\omega(k_m)$. Benjamin & Ursell (1954) delineate the various instability regions of the Mathieu equation for $\Gamma > 0$, their emergence arising for $\Gamma \geqslant 0$ at frequencies corresponding to integer multiples of half the driving frequency:

$$\omega_m = n\tfrac{1}{2}\omega_0, \quad n = 1, 2, \ldots. \tag{2.32}$$

In the inviscid case, the broadest instability tongue is the subharmonic mode, $n = 1$.

If one includes damping of the form we have discussed, and considers an unbounded setting to avoid difficulties related to a lateral no-slip condition on

cylinder walls, the dynamics will be governed by a damped Mathieu equation. This will result in a finite forcing threshold for the onset of instability. For this unbounded domain, there is a continuum of wavenumbers $\boldsymbol{k} = (k_1, k_2)$, and solutions of the form $\phi = a(\boldsymbol{k}, t)\mathrm{e}^{\mathrm{i}\boldsymbol{k}\cdot\boldsymbol{x}}\mathrm{e}^{|\boldsymbol{k}|z}$ where $\boldsymbol{x} = (x, y)$. The corresponding damped Mathieu equation takes the form

$$\frac{\mathrm{d}^2 a}{\mathrm{d}t^2} + 2\gamma \frac{\mathrm{d}a}{\mathrm{d}t} + [\omega^2 + \gamma^2 - \omega_g^2 \Gamma \cos(\omega_0 t)]\, a = 0, \tag{2.33}$$

where

$$k = |\boldsymbol{k}|, \quad \gamma(k) = 2\nu k^2, \quad \omega^2(k) = gk\left(1 + \frac{\sigma}{\rho g}k^2\right) \quad \text{and} \quad \omega_g^2(k) = gk. \tag{2.34a-d}$$

For this equation, the relation between k and Γ for neutral stability of the $n = 1$ mode (i.e. the subharmonic $\omega_0/2$ mode) is then given approximately (see appendix A) by the relation

$$[\omega^2 + \gamma^2 - \tfrac{1}{4}\omega_0^2]^2 + \omega_0^2\gamma^2 - \tfrac{1}{4}\omega_g^4\Gamma^2 = 0. \tag{2.35}$$

The most unstable wavenumber k can then be obtained by minimizing Γ with respect to k. Figure 1 shows the curve $\Gamma(k)$ for typical values used in experiments together with a comparison to the numerically observed thresholds obtained from time-dependent simulations of the system (2.26)–(2.28).

2.3. *Droplet trajectory and fluid coupling*

We now proceed to the fully coupled wave–droplet model. The fluid equations, presented above, must now include the pressure forcing P_D generated by the impacting droplet. The system takes the form

$$\Delta\phi = 0, \quad z \leqslant 0, \tag{2.36}$$

$$\phi \to 0, \quad \text{as } z \to -\infty, \tag{2.37}$$

$$\phi_t = -g(t)\eta + \frac{\sigma}{\rho}\Delta_H\eta + 2\nu\Delta_H\phi - \frac{1}{\rho}P_D(\boldsymbol{x} - \boldsymbol{X}(t), t), \quad z = 0, \tag{2.38}$$

$$\eta_t = \phi_z + 2\nu\Delta_H\eta, \quad z = 0, \tag{2.39}$$

where $g(t) = g(1 - \Gamma\cos(\omega_0 t))$.

The motion of the spherical droplet has two distinct stages, flight and impact. During flight, the droplet of mass m is in ballistic motion corrected by the aerodynamic force, which may be described in terms of Stokes drag in the horizontal direction (Moláček & Bush 2013b). The drop position is given by $(x, y, z) = (\boldsymbol{X}(t), Z(t))$ where $Z(t)$ is defined as the vertical position of the base of the droplet. Thus, in a frame moving with the vibrating container, the trajectory of the droplet in flight is governed by

$$m\frac{\mathrm{d}^2 Z}{\mathrm{d}t^2} = -mg(t), \tag{2.40}$$

$$m\frac{\mathrm{d}^2 \boldsymbol{X}}{\mathrm{d}t^2} = -6\pi R_0\mu_{air}\frac{\mathrm{d}\boldsymbol{X}}{\mathrm{d}t}, \tag{2.41}$$

where μ_{air} is the viscosity of air and R_0 is the drop radius. In the fluid equations, during flight, the applied surface pressure is set to zero, i.e. $P_D = 0$ in (2.38).
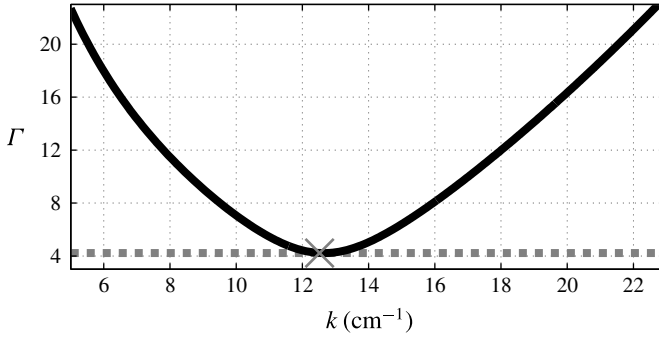
FIGURE 1. Approximate Faraday subharmonic stability curve (black) as predicted by (2.35) for the experimental parameters in appendix B. The viscosity of the fluid ν was adjusted to $\nu^* = 0.8025\nu$ so that the minimum of $\Gamma(k)$, as predicted by (2.35), matches the experimental value $\Gamma = 4.22$ reported in Wind-Willassen *et al.* (2013) and shown by the horizontal line. The minimum is achieved at $k_F = 12.64$ cm^{-1}. The cross indicates the numerically observed critical value for instability of (2.33), specifically $k_* = 12.52$ cm^{-1} at $\Gamma = 4.22$. The inverse Reynolds number for this case, based on ν^*, the Faraday frequency of $\omega_0/2$ and the associated Faraday wavelength λ^*, is $\epsilon \approx 0.016$.

The impact on the free surface begins at time $t = t_I$ when $\eta(X(t_I), t_I) = Z(t_I)$ and $d(Z - \eta)/dt|_{x=X} < 0$. During impact, the vertical dynamics is modelled as a nonlinear spring prescribed by the model of Moláček & Bush (2013b):

$$\left(1 + \frac{c_3}{\ln^2 \left| \frac{c_1 R_0}{Z - \bar{\eta}} \right|}\right) m \frac{d^2 Z}{dt^2} + \frac{4}{3} \frac{\pi \nu \rho R_0 c_2}{\ln \left| \frac{c_1 R_0}{Z - \bar{\eta}} \right|} \frac{d}{dt}(Z - \bar{\eta}) + \frac{2\pi\sigma}{\ln \left| \frac{c_1 R_0}{Z - \bar{\eta}} \right|}(Z - \bar{\eta}) = -mg(t),$$
(2.42)

while the horizontal trajectory is given by

$$m \frac{d^2 X}{dt^2} + \left(c_4 \sqrt{\frac{\rho R_0}{\sigma}} F(t) + 6\pi R_0 \mu_{air}\right) \frac{dX}{dt} = -F(t)\nabla \bar{\eta}|_{x=X}.$$
(2.43)

Details of the derivation of these equations are given in Moláček & Bush (2013b). In the equations for the vertical dynamics shown above, $\bar{\eta}$ denotes the hypothetical free-surface elevation that would exist in the absence of the current droplet impact. Thus, during the impact, two solutions to (2.38) and (2.39) are computed: the hypothetical one $\bar{\eta}$, $\bar{\phi}$ (where $\bar{\phi}$ is the velocity potential of this hypothetical flow) with $P_D = 0$ and 'initial value' $\bar{\eta} = \eta$, $\bar{\phi} = \phi$ at $t = t_I$; and another, denoted η, ϕ, which does include the pressure forcing due to the drop. This second solution is not explicitly used during the current impact, but captures the wave generation that will affect subsequent impacts. We note that in previous models (Oza *et al.* 2013; Moláček & Bush 2013b) the free-surface geometry is calculated without accounting for the current impact, whose effect on the wave field is included after the impact. Our model thus goes beyond its predecessors in explicitly computing the dynamic wave generation and propagation. A comparison between the waveforms predicted by the various models will be presented in § 3.3.

The constants c_1, c_2, c_3, c_4 are fixed: we carry out all single droplet experiments with values similar to those used in Moláček & Bush (2013*b*) and Wind-Willassen *et al.* (2013) (see appendix B). Briefly, c_1 prescribes the spring nonlinearity, c_2 the vertical component of damping, c_3 the drop's added mass induced during impact and c_4 the skidding friction. The right-hand side of (2.43) represents the propulsive force induced by the droplet's impact on the inclined surface at the impact location X. This impact force $F(t)$ experienced by the droplet is extracted from the vertical dynamics equation as

$$F(t) = \max \left[m \frac{\mathrm{d}^2}{\mathrm{d}t^2} Z + mg(t), 0 \right]. \tag{2.44}$$

The thresholding to prevent negative (suction) forces ($F(t) < 0$) was introduced on physical grounds in Moláček & Bush (2013*b*). The pressure is now given by

$$P_D = \frac{F(t)}{\pi R(t)^2}, \tag{2.45}$$

for $|\boldsymbol{x} - \boldsymbol{X}| < R(t)$ and $P_D = 0$ otherwise. Here $R(t)$ denotes the contact radius, which we model as

$$\pi R(t)^2 = \pi \min(2|Z - \bar{\eta}|R_0, (R_0/3)^2). \tag{2.46}$$

The lower bound is the leading-order approximation of the area of the base of the spherical cap resulting from intersecting the droplet with the horizontal plane of the unperturbed free surface, and the upper bound is an approximation guided by experimental observations. In applying (2.45) we have made the further approximation that the pressure forcing is spatially uniform over the impact area. We find that the model is not sensitive to changes in these approximations.

The impact ends at $t = t_E$, when $\bar{\eta}(X(t_E), t_E) = Z(t_E)$ and $\mathrm{d}(Z - \bar{\eta})/\mathrm{d}t|_{x=X} > 0$. At $t = t_E$, the 'bar' variables are discarded, then reinitialized at the beginning of the next impact. In summary, the evolution of $\bar{\eta}$ determines the drop dynamics, while the evolution of η accounts for the wave generation. A verification of the consistency of our model is that $\eta(X(t), t) \approx Z(t)$ during droplet impact, as is evident in the traces reported in figure 3.

3. Numerical modelling and simulations

For numerical efficiency, the horizontally unbounded domain is approximated with a large doubly periodic one, allowing the simple implementation of an accurate Fourier spectral method. The main goals of the numerical simulations are to capture the pilot-wave fields of single and interacting particles, and demonstrate the improvement in wave-field modelling relative to prior Bessel-function-based methods.

The system (2.38) and (2.39) is essentially two-dimensional, requiring only $\phi_z(\boldsymbol{x}, 0, t)$ (i.e. the irrotational vertical velocity) from (2.36). This calculation is simple in the doubly periodic domain where $\phi_z(\boldsymbol{x}, 0, t) = \mathscr{F}^{-1}[k\hat{\phi}(\boldsymbol{k}, t)]$, where $\hat{\phi} = \mathscr{F}[\phi(\boldsymbol{x}, 0, t)]$ and $\mathscr{F}$ and $\mathscr{F}^{-1}$ denote the Fourier transform and its inverse, respectively. This 'Dirichlet-to-Neumann' map amounts to calculating efficiently the vertical velocity at the free surface of a fluid from the horizontal velocity, when the velocity potential satisfies Laplace's equation in the bulk. In addition, for accuracy and efficiency, the full evolution equations (2.38) and (2.39) will be solved in Fourier space.

Through a numerical model and its corresponding computational simulations, we show that the coupled wave–droplet system (2.38), (2.39), (2.42) and (2.43) displays the key features of pilot-wave dynamics, specifically, wave generation and a myriad of bouncing and walking states, reported in laboratory experiments.

3.1. *The spectral method*

An accurate spectral method is used following the strategy of writing the evolution as a single complex equation as done by Milewski & Tabak (1999) and Wang & Milewski (2012). To sketch the method, consider the dimensionless form of the equations,

$$\phi_t = -\mathscr{G}(t)\eta + Bo\,\Delta_H\eta + 2\epsilon\,\Delta_H\phi - BoP_D(\boldsymbol{x}, t), \tag{3.1}$$

$$\eta_t = \phi_z + 2\epsilon\,\Delta_H\eta, \tag{3.2}$$

where the forcing pressure has been scaled with σ/λ, and time with the period of the subharmonic Faraday mode, resulting in $\mathscr{G} = G + \Gamma\cos(4\pi t)$.

In Fourier space, equations (3.1) and (3.2) are given by

$$\hat{\phi}_t = -[\mathscr{G}(t) + Bok^2]\hat{\eta} - 2\epsilon k^2\hat{\phi} - Bo\hat{P}_D(t), \tag{3.3}$$

$$\hat{\eta}_t = k\hat{\phi} - 2\epsilon k^2\hat{\eta}. \tag{3.4}$$

We perform the change of variables

$$\hat{u} = \hat{\eta} + \mathrm{i}\frac{k}{\omega}\hat{\phi}, \tag{3.5}$$

where

$$\omega(k) = \sqrt{k(G + Bok^2)}. \tag{3.6}$$

The system is then easily integrated, for each k, as a single linear complex equation. The part of the equation that has constant coefficients can be integrated exactly, and then the evolution of the Fourier amplitudes amounts to

$$\frac{\mathrm{d}}{\mathrm{d}t}[\hat{u}\mathrm{e}^{(\mathrm{i}\omega+2\epsilon k^2)t}] = -\mathrm{i}\frac{k}{\omega}(\Gamma\cos(4\pi t)\hat{\eta} + Bo\hat{P}_D(t))\mathrm{e}^{(\mathrm{i}\omega+2\epsilon k^2)t}. \tag{3.7}$$

In the absence of both vibration ($\Gamma = 0$) and pressure forcing ($P_D = 0$), no numerical integration is needed. In the presence of these effects, equation (3.7) is solved using a fourth-order Runge–Kutta method. The original variables are recovered from $\hat{u}$ by decomposing expression (3.5) into its Hermitian and skew-Hermitian parts and inverting it. As explained earlier, during contact time, the averaged free surface $\bar{\eta}$ and its slope $\nabla\bar{\eta}$ feed into the droplet dynamics (2.42) and (2.43) and are obtained by integrating the wave equations with $P_D = 0$. The vertical dynamics and trajectory ordinary differential equations (2.40)–(2.43) are also solved directly by a Runge–Kutta method, and provide the coupling pressure P_D through (2.44) and (2.45). To model accurately the full impact, we must resolve a multiscale problem, with scales ranging from the penetration depth, of $O(0.1\ \mathrm{mm})$, to the characteristic wavelength of the pilot wave, of $O(1\ \mathrm{cm})$. In our single-drop computations we typically use 1024×1024 Fourier modes in space.

In what follows, we present a series of numerical simulations confirming that the system of differential equations (2.38)–(2.43) is capable of generating much of the complex behaviour reported in laboratory experiments.
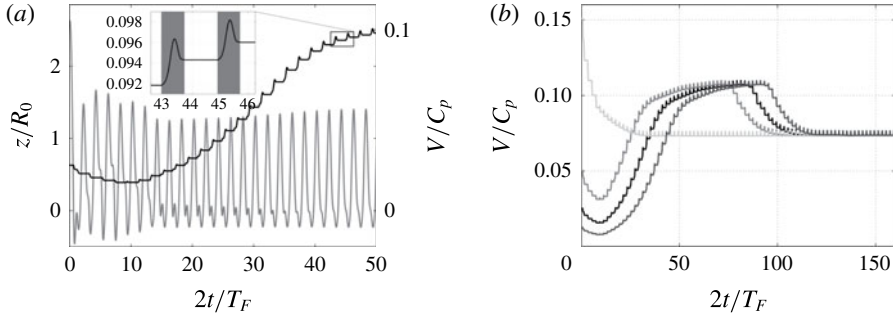
FIGURE 2. (*a*) Evolution of the droplet's horizontal velocity (V/C_p, black) and elevation above the free surface (z/R_0, grey), in the bath's frame of reference. Following its release onto the surface at a low speed, the droplet decelerates, then accelerates towards its steady walking speed. The inset shows the velocity variations over the Faraday period, reflecting the two stages of the drop motion, impact (grey) and free flight. (*b*) Evolution of the walker dynamics from different initial conditions. After an initial transient, all walkers converge on an identical walking state with the same impact phase.

3.2. *Dynamics of single drops*

We first investigate the bifurcations between different walking and bouncing states as reported by Protière *et al.* (2006), Eddi *et al.* (2008, 2011), Moláček & Bush (2013*a*,*b*) and Wind-Willassen *et al.* (2013). In the laboratory experiments, a droplet is released onto a vibrating bath of silicone oil. Depending on the forcing acceleration Γ, the droplet may coalesce, bounce or walk, propelled by its own pilot wave. We proceed by comparing the experimental observations with the predictions of our model.

Following Moláček & Bush (2013*a*), we characterize the system in terms of the dimensionless driving acceleration, Γ/Γ_F, and the vibration number, Ω. For given Γ/Γ_F and Ω values, we initialize a computation by releasing a particle onto the fluid surface at a low horizontal speed. Below the walking threshold, for $\Gamma < \Gamma_W(\Omega)$, the particle quickly comes to rest, and settles into a stationary bouncing mode. When $\Gamma > \Gamma_W(\Omega)$ the particle accelerates and settles into a steady walking state (see figure 2). Our model exhibits hysteresis, which can be observed, for example, by choosing different values of the initial particle speed. In the experiment shown in figure 2(*b*), the initial velocity does not affect the final steady speed. For $\Omega = 0.8$ and $3.55 < \Gamma < 3.7$, however, either the $(2, 1)^1$ or $(2, 1)^2$ state may emerge, depending on the initial velocity. Qualitatively similar hysteretic effects were observed in the experiments of Wind-Willassen *et al.* (2013), but not quantified. In the remainder of the paper, for simplicity, we consider only the long-time behaviour arising from low initial velocities. In certain cases, particularly when $\Gamma \approx \Gamma_F$, the walking appears to be irregular and chaotic, at least over the times that we compute. We recall that our wave model has only one adjustable parameter, the effective viscosity of the fluid. Using the real viscosity of the fluid overestimates the experimental Faraday threshold by approximately 20 %. We thus adjust the viscosity in order to match this threshold (see figure 1). The parameters c_j governing the droplet dynamics (2.42) and (2.43) are similar to those used in Moláček & Bush (2013*b*) and Wind-Willassen *et al.* (2013), but are slightly modified in order to match the experimentally observed walking threshold, Γ_W (see appendix B). The walking threshold Γ_W is most sensitive to the
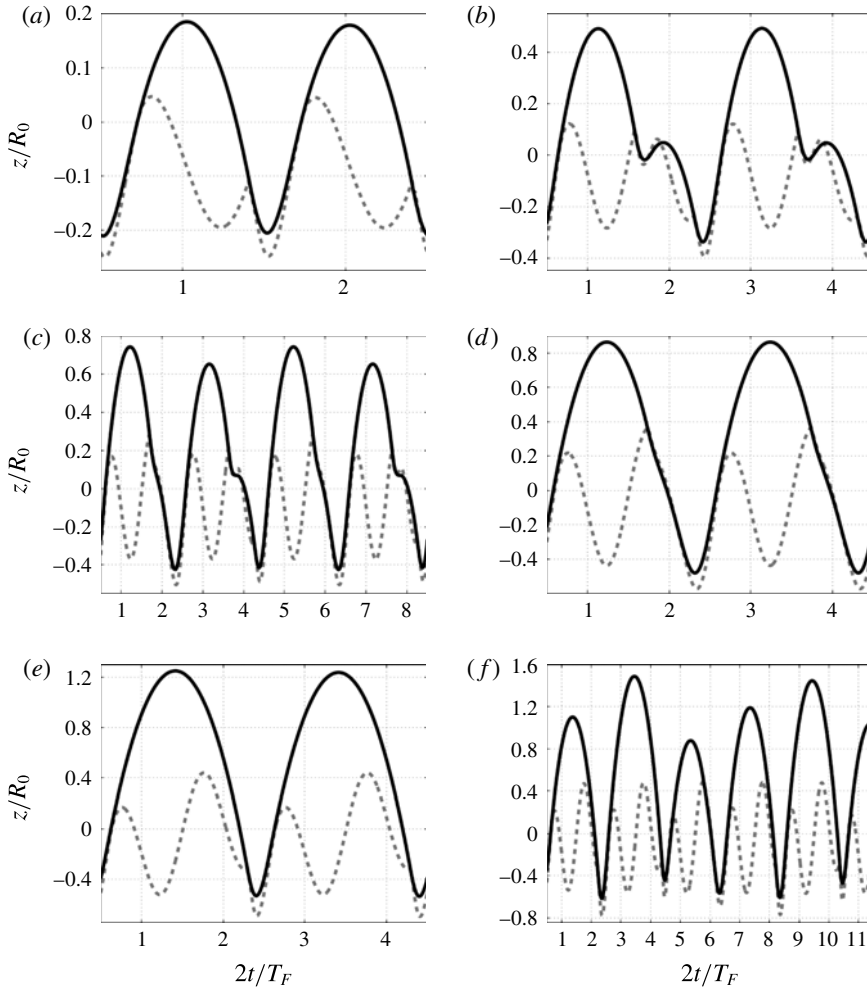
FIGURE 3. Vertical dynamics of the $(m, n)^p$ bouncing and walking modes: (*a*) $(1, 1)$ bouncing at $\Gamma = 1.6$; (*b*) $(2, 2)$ bouncing at $\Gamma = 2.3$; (*c*) $(4, 3)$ bouncing at $\Gamma = 2.9$; (*d*) $(2, 1)^1$ walking at $\Gamma = 3.4$; (*e*) $(2, 1)^2$ walking at $\Gamma = 3.8$; and (*f*) chaotic walking at $\Gamma = 4.15$. The vertical position of the droplet's lowermost point is indicated by the solid line and the height of the underlying bath by the dashed line. The panels indicate elevations relative to the non-vibrating laboratory frame of reference. The horizontal axis is in units of forcing periods ($T_F = 1/80$ s), and the vertical axis in units of drop radii. All experiments shown correspond to $\Omega = 0.8$, i.e. a drop radius of $R_0 = 0.38$ mm forced by a bath vibrating at 80 Hz. The Faraday threshold is $\Gamma_F = 4.22$.

skidding friction parameter c_4, which was chosen such that the walking threshold matched that observed experimentally. For the other parameters, the dynamics is most sensitive, in decreasing order, to c_1, c_3 and c_2.

Detailed regime diagrams in the $\Omega - \Gamma / \Gamma_F$ plane were presented in Moláček & Bush (2013*a*,*b*) and Wind-Willassen *et al.* (2013). We adopt their nomenclature, labelling different bouncing and walking states with a triplet of integers $(m, n)^p$, where m is the number of forcing periods and n the number of bounces in one overall bouncing cycle. If there is a multiplicity of (m, n) modes, p ranks them according to their relative

mechanical energies, $p = 1$ being the lowest. For example, $(4, 2)$ signifies a motion that repeats every four forcing periods and consists of two different bounces; otherwise, it would be a $(2, 1)$ mode.

In figure 3, various simulated bouncing modes are displayed. The vertical position of the lowermost point of the droplet and the free-surface elevation beneath the droplet centre are shown as a function of time for fixed Ω and several values of Γ. Both bouncing and walking states are represented. At a few points we note a slight inconsistency between the free-surface elevation and the droplet position during impact; specifically, the droplet appears to cross the interface. In reality, the droplet and the waves are separated by a thin lubrication layer of air that transmits normal stresses between the two. In our model, the fluid is free to respond to the pressure field of the droplet and we do not impose their relative positions. During most of the contact time, the solid and dashed lines coincide. The extent of this discrepancy, that is, the crossing of the drop and bath surfaces, thus provides a measure of the consistency of our model.

Figure 3 also indicates how the system transitions between the various modes. For example, a fundamental difference between the $(2, 1)^1$ and $(2, 1)^2$ modes (cf. panels *d* and *e*) is the droplet impact phase. In figure 4, the behaviour of our model is shown in the Ω–Γ plane and compared directly to the experimental results of Wind-Willassen *et al.* (2013) (see their figure 3). The vibration number Ω was varied in our simulations by changing the droplet radius. The predicted dynamical states are indicated by the background colour and the laboratory experiments are shown by the colour-coded points, squares for bouncers and circles for walkers. Evidently, our numerical model is able to adequately capture the diversity of bouncing modes and their transition points, with only relatively small deviations from the experimental results. The main quantitative differences are that the extent of our predicted walking region (as indicated by the red curve) is relatively large, and that the $(2, 1)^1$ to $(2, 1)^2$ transition occurs at a slightly higher forcing amplitude.

In figure 5, details of the dynamics for a horizontal slice through figure 4 at $\Omega = 0.8$ are shown. Specifically, it indicates the dependence of the walking speed, impact phase and walking mode on the vibrational forcing. The impact phase and speed show a characteristic decrease at the transition between the $(2, 1)^1$ and $(2, 1)^2$ modes, consistent with the observations and theoretical predictions of Moláček & Bush (2013*b*). We recall that the variations of the drop's walking speed, arising over the Faraday period due to its distinct phases of impact and free flight, are shown in figure 2.

3.3. *The walker-induced wave field*

Previous theoretical models of the wave field have used a superposition of waves generated by preceding impacts,

$$\eta(\boldsymbol{x}, t) = \sum_n h_n(\boldsymbol{x}, t), \qquad (3.8)$$

where h_n is the wave generated by the *n*th prior impact at time t_n. Two models for h_n have been used for bouncing and walking studies. Eddi *et al.* (2011) proposed a cosine form with both spatial and temporal damping,

$$h_n(\boldsymbol{x}, t) = \frac{A}{|\boldsymbol{x} - \boldsymbol{X}(t_n)|} \cos(k_F |\boldsymbol{x} - \boldsymbol{X}(t_n)| + \phi) \mathrm{e}^{-|\boldsymbol{x} - \boldsymbol{X}(t_n)|/\delta} \mathrm{e}^{-(t - t_n)/T_F M_e}, \qquad (3.9)$$
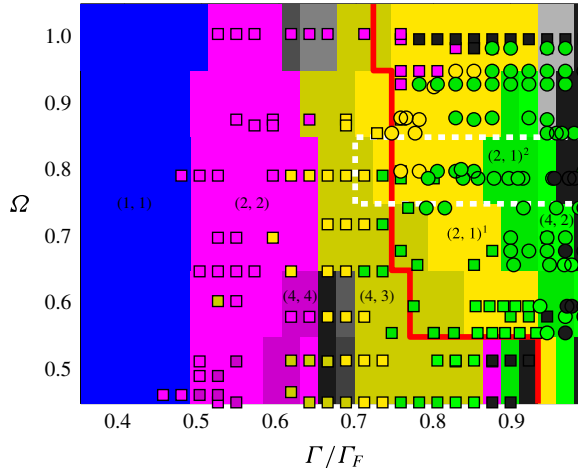
FIGURE 4. Regime diagram indicating the form of the bouncing behaviour in the Γ/Γ_F–Ω plane, where $\Omega = \omega_0 \sqrt{\rho R_0^3/\sigma}$ is the vibration number. Squares (bouncing modes) and circles (walking modes) are laboratory data reported by Wind-Willassen *et al.* (2013). The background is tiled in rectangles of size 0.1×0.1, coloured according to the $(m, n)^p$ mode predicted to arise at the centre of the tile. The square and round markers follow the same colour scheme as the background. The red line indicates the predicted transition between bouncing and walking predicted by our model. Black regions represent chaotic bouncing or walking, and grey regions indicate that the period of droplet motion is equal to or greater than six forcing periods. The changes in velocity and bouncing phase in the region delimited by the white dashed lines are indicated in figure 5.

in which δ is a decay length parameter. They also introduce a Bessel function model for the surface evolution. Moláček & Bush (2013*b*) derived a form valid in the small-drop limit,

$$h_n(\boldsymbol{x}, t) = \frac{A}{\sqrt{t - t_n}} J_0(k_F|\boldsymbol{x} - \boldsymbol{X}(t_n)|) e^{-(t-t_n)/T_F M_e} \cos(\omega_0 t/2), \qquad (3.10)$$

where the memory parameter $M_e = T_d/T_F(1 - \Gamma/\Gamma_F)$ depends on the proximity to threshold, as well as the decay time of the unforced waves, T_d. We note that a memory parameter does not arise in our formulation, since we solve explicitly for the full wave field. However, an asymptotic value for the decay rate in our model, from which one may infer an analogue to the memory parameter, is provided in appendix A. The $\sqrt{t}$ decay factor arising in the narrow-band asymptotic analysis of Moláček & Bush (2013*b*) is omitted in some other models of the surface waves (e.g. Oza *et al.* 2013) for the sake of simplicity. Asymptotic values for the amplitude parameter A and damping time $T_d = T_F M_e$ appearing in (3.10) are given in Moláček & Bush (2013*b*).

Figure 6 illustrates the numerically predicted wave fields generated by a drop impacting the surface in the absence and presence of vibrational forcing. It may be compared directly to the wave fields reported in figure 4 of Eddi *et al.* (2011). In the absence of vibrational forcing, a transient wave sweeps radially outwards from the point of impact. With vibrational forcing, this transient serves to trigger a standing field of Faraday waves that persists in its wake, decaying with time. In the forced experiments, both the transient wave speed and the spatial form of the excited
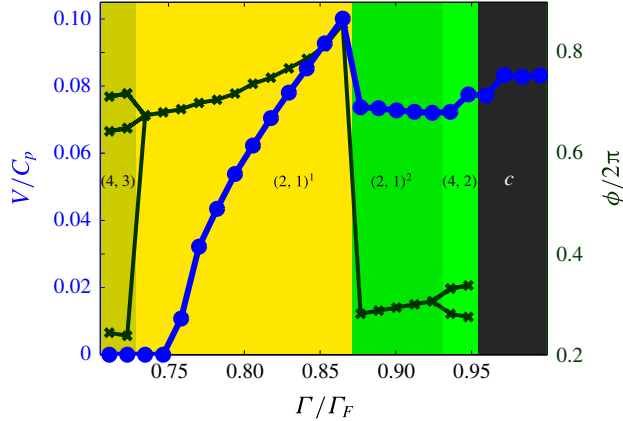
FIGURE 5. The dependence of impact phase ϕ and horizontal speed V on the vibrational forcing Γ/Γ_F for $\Omega = 0.8$, along the region delimited by the dashed white lines in figure 3. The blue line indicates V/C_p, where C_p is the phase speed of a wave with the Faraday wavelength. The black lines indicate the impact phase ($\phi/2\pi$). The background colours correspond to the different bouncing and walking modes, as indicated in figure 4. For $\Gamma/\Gamma_F \lesssim 0.75$, the particle is bouncing in either the $(4, 3)$ mode or the $(2, 1)$ mode. The bouncer then transitions to a walking state. The phase curve takes multiple values in regimes with more than one bounce per period. A characteristic jump in both phase and speed identifies the transition between the $(2, 1)^1$ and $(2, 1)^2$ walking modes.

standing wave are independent of the vigour of the vibrational forcing. The spatial form is very close to the Bessel function $J_0(k_F r)$, particularly for later times (see figure 7). The measured speeds of the sweeping front for the experiments shown in figure 6 are 18.59, 19.45, 19.73 and 20.04 cm s^{-1} for $\Gamma = 0$, 3.15, 3.6 and 4.15, respectively. For the cases with vibrational forcing, the speed is very close to the Faraday phase speed of 20.07 cm s^{-1}. For the unforced experiment, the speed is somewhat less, and is set by least slowly damped waves excited by the impact. In this case, the speed is bounded below by the minimum gravity–capillary wave speed, $\sqrt{2}(\sigma g/\rho)^{1/4} \approx 17.1$ cm s^{-1}.

Figure 8 shows the cross-sectional free-surface height of a $(2, 1)^1$ bouncer at the moment before impact, as predicted by a number of theoretical models. Figure 9 shows a comparison between our numerical wave profile, and the Bessel approximations of Moláček & Bush (2013b) without and with a spatial damping term. The spatial damping follows from expression (3.10) due to Moláček & Bush (2013b) (see their equations (A46) for β_1 and (A47)), which has an $O(r^2/4\beta_1\tau)$ correction term arising from an expansion of $\exp(-r^2/4\beta_1\tau)$. When this correction is applied, each Bessel function is multiplied by a Gaussian radial profile. These results highlight the role of exponential spatial decay on the walker's wave field.

In figure 10, we show the dependence of the spatial decay length of the bouncers and walkers on Γ, as computed by factoring out the $r^{-1/2}$ spatial decay factor of the $J_0(k_F r)$ Bessel function. Specifically, we took the modulus of every maximum and minimum transverse to the walking direction and fitted it to a curve of the form $Ar^{-1/2}\exp(-r/L_d)$. The spatial decay length increases between $1.5\lambda_F$ and $4\lambda_F$ as Γ is increased progressively. We note that the only experimental spatial decay length reported in the literature is the $1.6\lambda_F$ mentioned by Eddi *et al.* (2011).
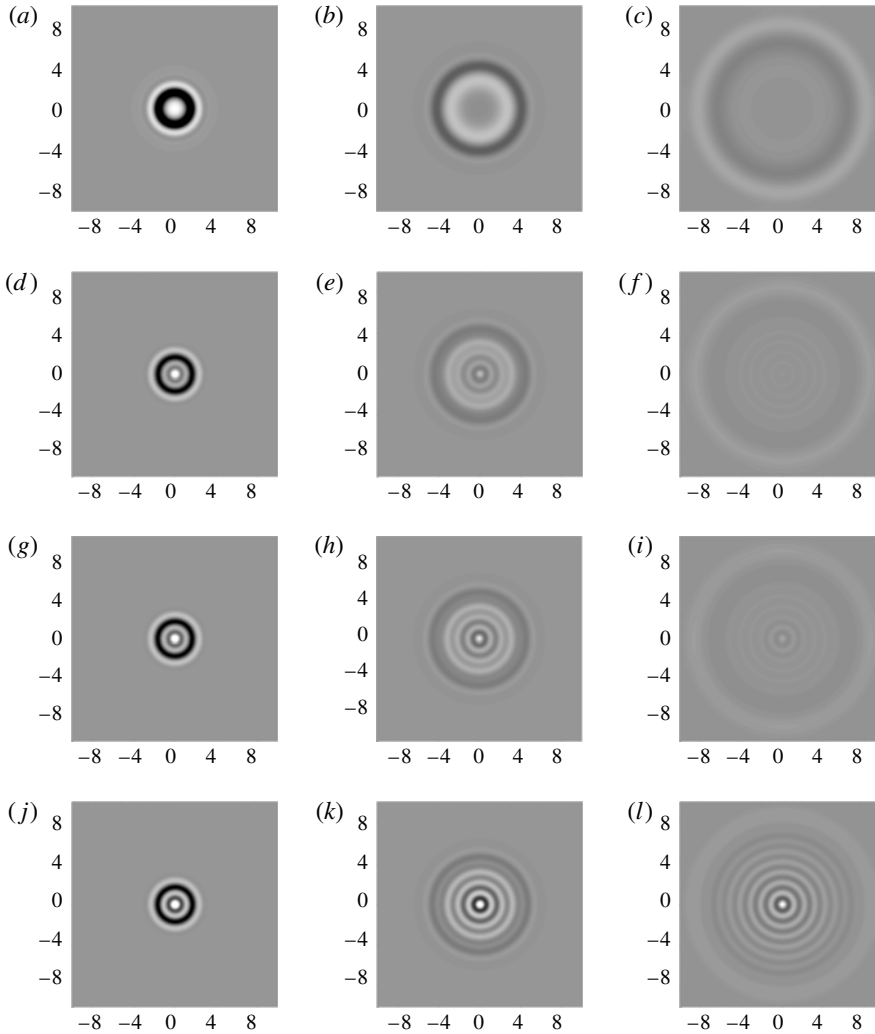
FIGURE 6. The computed wave fields generated by a single drop impact on a quiescent bath (*a–c*), and a bath vibrating at $f = 80$ Hz with $\Gamma = 3.15$ (*d–f*), $\Gamma = 3.6$ (*g–i*) and $\Gamma = 4.15$ (*j–l*). The wave field was generated by a single impact of a drop of $R_0 = 0.38$ mm and density 10 times that of the bath. The axes are labelled in units of Faraday wavelengths. Images are taken at times $t = 2T_F$ (*a,d,g,j*), $t = 6T_F$ (*b,e,h,k*) and $t = 11T_F$ (*c,f,i,l*) after impact, where T_F is the Faraday period.

Figure 11 shows the time evolution of the free surface arising from the same $(2, 1)^1$ bouncer as in figure 8 over the course of a Faraday period. While the Bessel model is constructed as a standing wave, our solution clearly generates a wave that propagates away from the impact centre as evidenced by the V-shaped furrow in figure 11(*b,c*). We note that the full temporal wave field of the Bessel approximation has been used in a variety of situations, for example, in chaotic bouncing (Moláček & Bush 2013*b*).

The Doppler shift along a walker's wave field is displayed in figure 12(*a*). The solid line shows the free surface along the direction of motion, and the dashed line that in the transverse direction. The Doppler shifting is evidenced by the changing
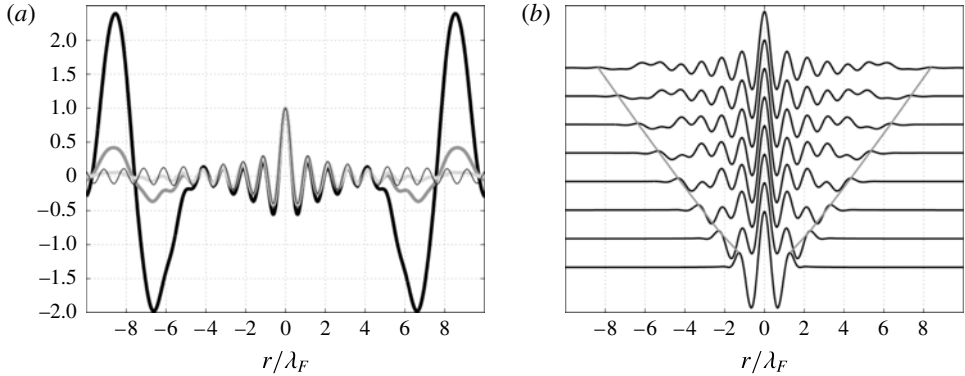
FIGURE 7. (*a*) Cross-sections of wave fields generated by single impact corresponding to figure 6(*f*) (black), (*i*) (grey) and (*l*) (light grey), normalized to have the same height at the origin. The thin line corresponds to a Bessel function $J_0(k_F r)$. (*b*) Cross-sections of the single-impact free surface for $\Gamma = 4.15$ at times $t = T_F, 2T_F, \ldots, 8T_F$ scaled so as to have the same height at the origin. The line indicates the leading edge of the disturbance. The horizontal axes show distance from the point of impact.
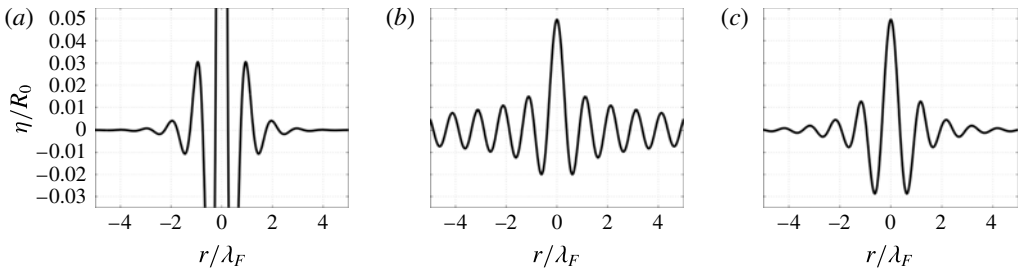
FIGURE 8. Different model predictions of the free-surface cross-section of a $(2, 1)^1$ bouncer at the moment before impact with $\Gamma = 3.1$. (*a*) The cosine wave model (3.9) of Eddi *et al.* (2011) with a spatial damping with decay length $1.6\lambda_F$ reported by the authors. Note the singularity at $r = 0$. (*b*) The Bessel model (3.10) of Moláček & Bush (2013*b*). (*c*) The result of our computation.

distance between crests on the two curves. Figure 12(*b*) shows the dependence of the Doppler shift on the walker's mean velocity, along with the experimental results of Eddi *et al.* (2011). While the Bessel-function-based models have been successful in describing certain aspects of the problem, they cannot capture the Doppler shift due to the moving wave maker. This arises from the fact that the Bessel function $J_0(k_F r)$ can be written as the superposition of plane cosines of fixed wavelength $2\pi/k_F$ in every direction, centred at the origin:

$$J_0(r) = \frac{1}{\pi} \int_{-\pi/2}^{\pi/2} \cos(r \cos\theta) \, d\theta. \tag{3.11}$$

Therefore the function $J_0(k_F r)$ in the (x, y) plane does not contain wavelengths other than $2\pi/k_F$. Physically, this is the wavelength observed in all directions as r becomes large. Alternatively, the spectrum $\hat{J}_0(\boldsymbol{k}/k_F)$ is non-zero only on the circle $k = k_F$ in the (k_1, k_2) plane.
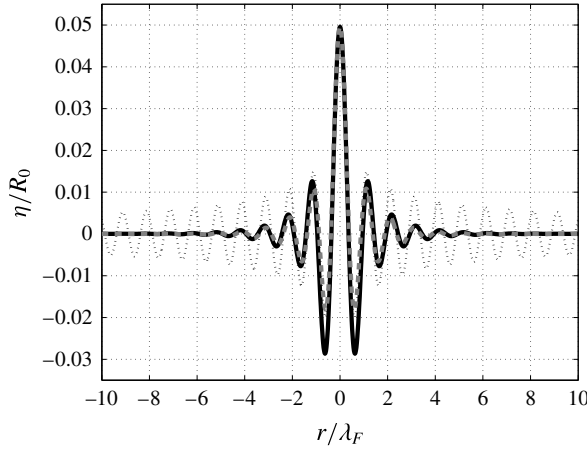
FIGURE 9. Comparison between the wave-field predictions of the present model (black curve) with those of Moláček & Bush (2013*b*) without (dotted curve) and with (grey dashed curve) the higher-order spatial damping correction suggested by Moláček & Bush (2013*b*) to the Bessel model (3.10).
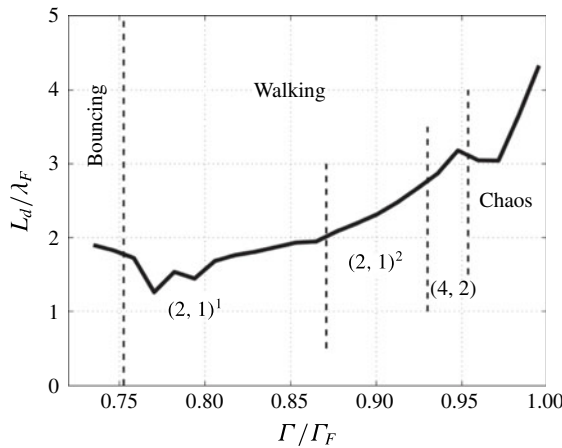

FIGURE 10. Computed dependence of the dimensionless decay length (L_d/λ_F) on the vibrational forcing Γ. Here, $\Omega = 0.8$. As Γ is increased, the bouncer evolves into a walker with the gaits indicated.

The free-surface elevation of a $(2, 1)$ walker with straight-line trajectory $X = (V(t - \phi), 0)$ with impacts at $t_n = -2nT_f + \phi$ and observed immediately before an impact at $t = \phi$ is

$$\eta = A \sum_{n=1}^{\infty} \frac{\mathrm{e}^{-2n/M_e}}{\sqrt{2nT_f}} \cos\left[\pi \frac{\phi}{T_f}\right] \mathrm{J}_0(k_F |(x + 2nVT_f, y)|). \tag{3.12}$$

Its Fourier transform is given by

$$\hat{\eta} = A \cos\left[\pi \frac{\phi}{T_f}\right] \hat{\mathrm{J}}_0(\boldsymbol{k}/k_F) \sum_{n=1}^{\infty} \frac{\mathrm{e}^{-2n/M_e}}{\sqrt{2nT_f}} \mathrm{e}^{-\mathrm{i}k_1 2nVT_f}, \tag{3.13}$$
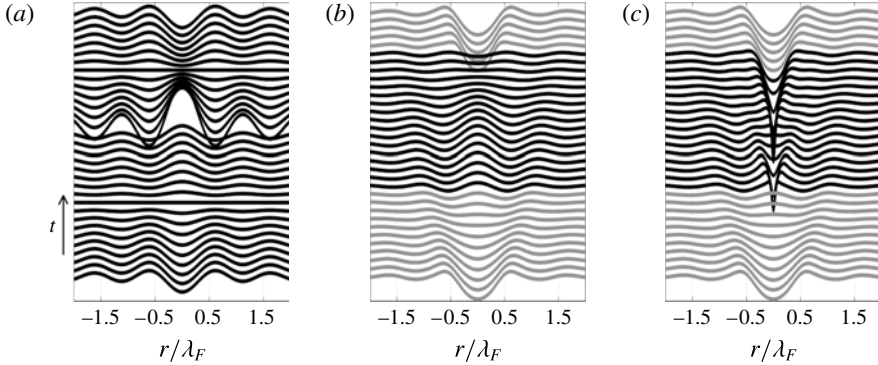
FIGURE 11. The time evolution of the free surface through the course of a Faraday period for the same bouncer as in figure 8. (*a*) The model of Moláček & Bush (2013*b*), as described by equation (3.10). The discontinuity arises when the surface is updated by the addition of a new Bessel function. (*b*) Our model's prediction, $\bar{\eta}$, for the free surface in the absence of the current impact. The dark curves correspond to wave forms arising when the drop is in contact with the bath, the lighter curves to times when the drop is in flight. (*c*) Our model prediction for the free surface when the current droplet impact is included.
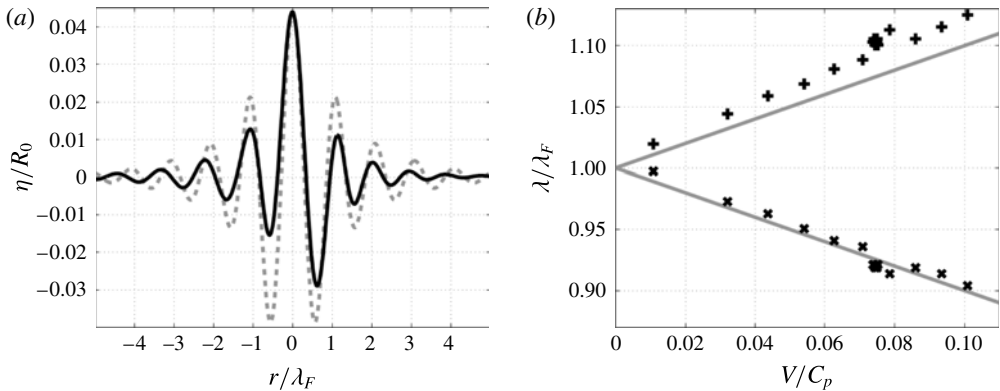
FIGURE 12. (*a*) The Doppler effect arising at $\Omega = 0.8$, $\Gamma = 3.6$. The solid line shows the surface along the direction of motion, the dashed line that in the transverse direction. The horizontal axis is in units of Faraday wavelengths, and the vertical axis in units of drop radii. (*b*) The Doppler effect displayed ahead and behind the walker, with λ/λ_F (vertical axis) in terms of V/C_p. The $\times$ markers depict the wavelength ahead of the walker, the $+$ markers the wavelength behind it. The lines indicate the magnitude of the Doppler effect reported by Eddi *et al.* (2011). Here V is the mean walker speed and C_p the phase speed.

where $\hat{J}$ is the Fourier transform of J, and $\mathbf{k} = (k_1, k_2)$. This formula shows that according to this Bessel-function model, the spectrum of the full wave field is equal to the spectrum of the single Bessel function $J_0(k_F r)$ multiplied by a function of k_1. The wave field thus contains energy only at the wavelength $2\pi/k_F$, and the mathematical form (3.12) cannot capture a Doppler shift. Figure 13 shows the Fourier spectrum of the numerical wave field for a walker immediately before the drop strikes the surface. By way of comparison, the spectrum of (3.12) would lie only on the circle in the figure.
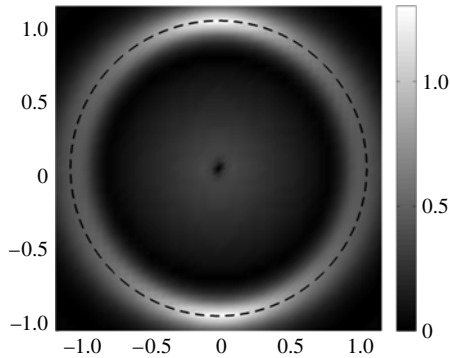
FIGURE 13. Amplitude of the Fourier spectrum of the computed wave field for a walker immediately before the drop impacts the surface. A superposition of Bessel functions $J_0(k_F r)$ would have a spectrum only on the dashed circle of radius k_F. It is the frequency spread of the spectrum about this circle that allows for a Doppler shift in the wave field. Axes are in units of inverse Faraday wavelengths.

Finally, typical wave fields computed from our single-droplet simulations are shown in figure 14. These are consistent with the laboratory images presented in Eddi *et al.* (2011), as well as the stroboscopic model predictions of Oza *et al.* (2013). Figure 14(*d*) shows that, when the walker moves rapidly to the right, an interference pattern appears in its wake.

3.4. *Two-particle interaction*

The generalization of our model to numerous walkers is straightforward, so we do not present it in detail. The additional ingredient is the computation of a mean free-surface elevation $\bar{\eta}_j$ for each particle during the fluid impact. This elevation incorporates the waves due to the impact of all other particles. Hence, in computing $\bar{\eta}_j$, we take the pressure in (2.38) to be

$$\sum_{i \neq j} P_{D,i}(\boldsymbol{x} - \boldsymbol{X}_i(t), t). \tag{3.14}$$

We proceed by investigating the interaction between a pair of walkers, as was examined experimentally by Protière *et al.* (2006), Protière, Bohn & Couder (2008) and Eddi *et al.* (2012). We confine our attention to two special cases, where the walkers are initially antiparallel and parallel. Protière *et al.* (2008) report that when the walkers are initially antiparallel, and so approach each other, they may either scatter or lock into orbit, depending on their relative bouncing phase, and the perpendicular distance between their original paths, the so-called impact parameter, d_I.

In the scattering regime, wave forces on the droplets causes them to repel. Conversely, in the orbiting regime, the droplet pair forms a stable and well-defined association bound together by their superposed pilot waves. In figure 15, orbiting and scattering of in-phase droplets are shown. Orbital states obtained by varying Γ for in- and out-of-phase walkers are shown in figure 16. The orbits are stable (i.e. persistent after extended computations) and can have different forms (circular, periodic wobbling or chaotic wobbling) depending on the system parameters, particularly the forcing amplitude Γ. Note that the in-phase orbiters have an orbital diameter of approximately
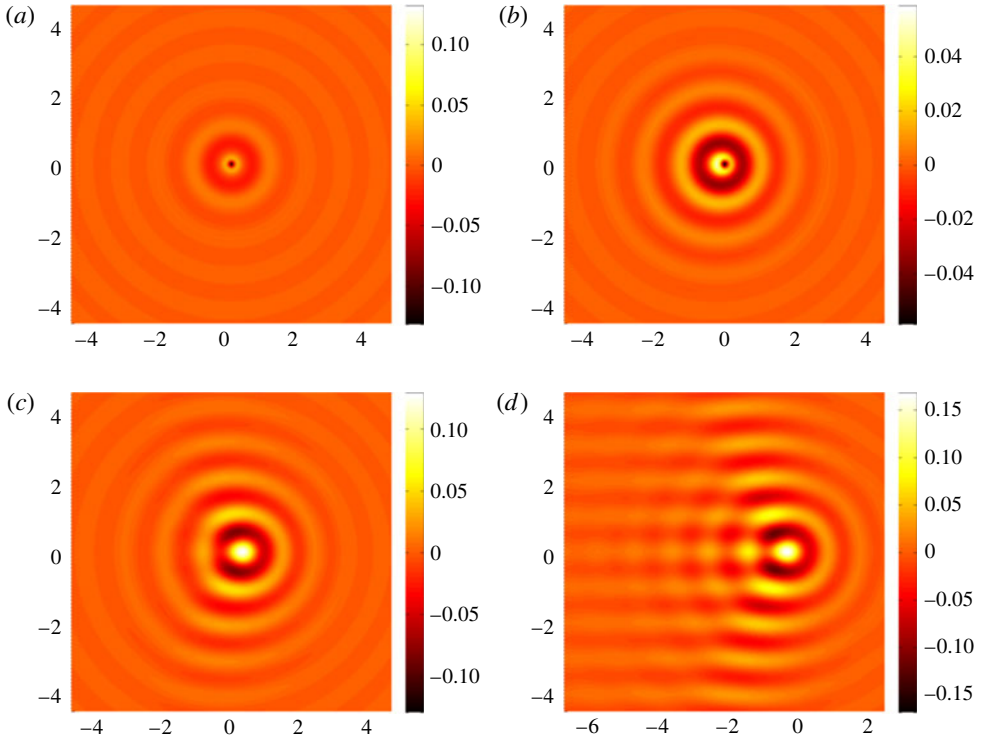
FIGURE 14. (Colour online) Wave fields accompanying bouncing and walking drops. (a) At $\Gamma = 3.1$, the axisymmetric wave field of a bouncer arises. At (b) $\Gamma = 3.3$, (c) $\Gamma = 3.8$ and (d) $\Gamma = 4.15$, walkers of progressively increasing speed arise, their wave fields being progressively more fore–aft asymmetric. Axes are in units of Faraday wavelengths, and the surface elevation (side bar) is in units of drop radii. In all panels, the drop is at the origin and (except for a) moving to the right. The simulations were performed with drops of $\Omega = 0.8$ (i.e. $R_0 = 0.38$ mm), for $\Gamma_W = 3.15$.

$0.8\lambda_F$; the out-of-phase orbiters approximately $1.3\lambda_F$. This difference may be roughly understood on the grounds that orbiters are more stable when bouncing in the troughs than on the crests of their partner's wave field.

When the walkers are initially parallel, they may lock into a 'promenade mode', in which they walk in unison, but the distance between them oscillates periodically (figure 17). After an initial transient, a well-defined periodically oscillating walking state emerges. This promenade mode and the characteristic oscillations in speed are both readily observed in the laboratory, and have recently been investigated by Borghesi *et al.* (2014).

4. Conclusions

We have developed a model of pilot-wave hydrodynamics that utilizes a self-consistent treatment of the generation and propagation of the walker's Faraday wave field. Specifically, the walker is described through coupling the droplet and its wave, the vertical motion of the former serving as the source of the latter. The waves are described as deep-water Faraday waves wherein the dissipation occurs in a viscous boundary layer at the free surface. Like the model of Moláček &
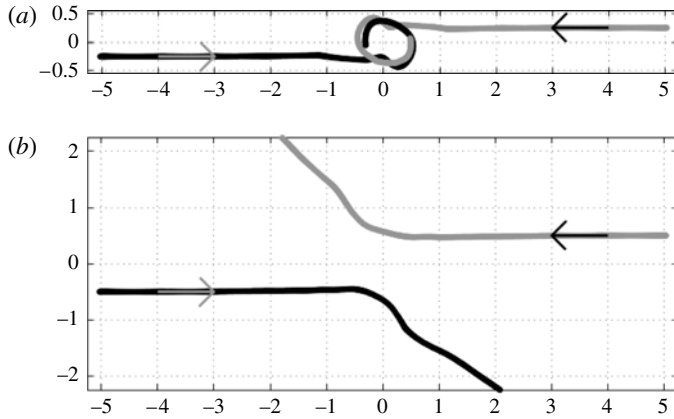
FIGURE 15. Collisions of in-phase droplet pairs. (*a*) With impact parameter of $d_I = 0.5\lambda_F$, the pair are captured in a periodic orbit with a diameter of approximately $0.5\lambda_F$. (*b*) With an impact parameter $d_I = \lambda_F$, the droplets scatter. Vertical and horizontal length scales are in units of λ_F.
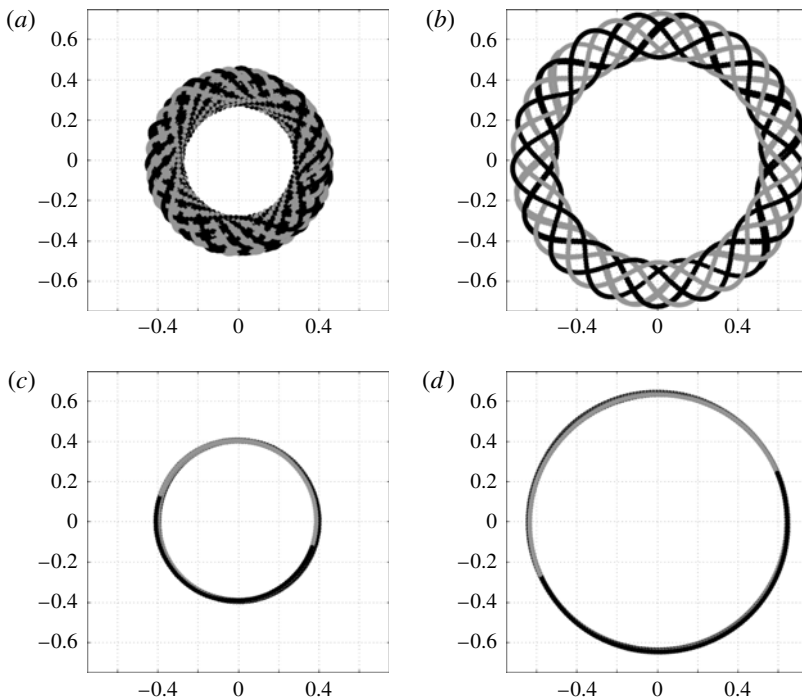

FIGURE 16. Orbital modes arising through walker–walker interactions, specifically from a pair of identical walkers launched with antiparallel velocity. Bouncing in phase with (*a*) $c_4 = 0.32$, $\Omega = 0.8$, $\Gamma = 3.7$ and (*c*) $c_4 = 0.3$, $\Omega = 0.7$, $\Gamma = 4$. Bouncing out of phase with (*b*) $c_4 = 0.32$, $\Omega = 0.8$, $\Gamma = 3.6$ and (*d*) $c_4 = 0.3$, $\Omega = 0.7$, $\Gamma = 4$. Axes are in units of the Faraday wavelength. Note the offset of orbital radii between the in- and out-of-phase walkers.
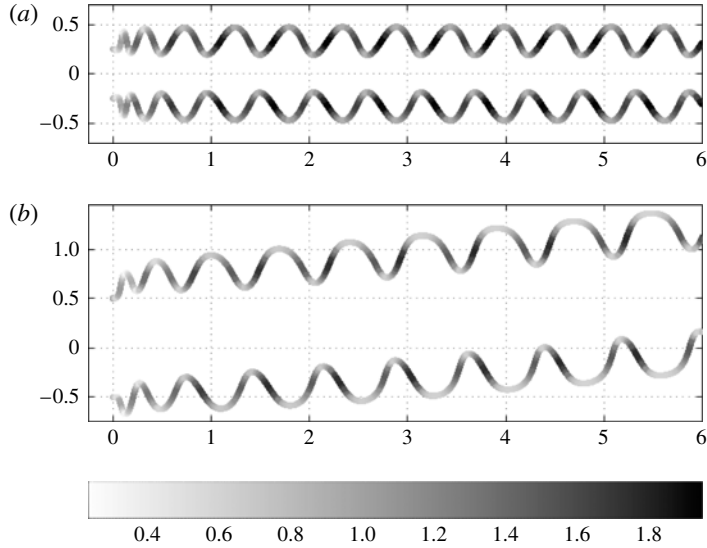
FIGURE 17. Droplet pair forming a stable 'promenade mode'. Two identical droplets propagate together in a given direction while oscillating in the transverse direction. Axes are in units of the Faraday wavelength. Two walkers bouncing (*a*) in phase and (*b*) out of phase. The instantaneous speed V/C_p is colour-coded according to the grey scale bar. The mean speeds of the promenading pair in panels (*a*) and (*b*) are 0.88 and 0.63 of the single-walker free walking speed, respectively.

Bush (2013*a*,*b*), it explicitly considers the bouncing phase through consideration of a vertical dynamics; thus, it is able to reproduce the observed dependence of the bouncing and walking modes on the system parameters. This gives it a marked advantage over the stroboscopic model presented by Oza *et al.* (2014*a*,*b*), wherein the effects of variable bouncing phase are not considered. Its additional advantage over the model of Moláček & Bush (2013*b*) is that it captures more accurately the wave field, including the transient wave field that serves as the precursor to the stationary wave field, as may play a significant role in the interaction of walkers with boundaries or other walkers.

   We have demonstrated that the model reproduces certain features of walker–walker interactions that have not been comprehensively studied with previous models, including orbiting, scattering and the promenade mode. For these interactions, the dependence of the system behaviour on the impact phase has been highlighted. In particular, we have seen that the scattering behaviour of a pair of walkers depends on both the impact parameter and the relative phase of the walkers. A quantitative comparison between our model predictions and an ongoing experimental investigation of walker–walker interactions will be presented elsewhere.

   Through its relatively complete treatment of the wave field, our model provides a platform for examining the interaction of walkers with boundaries, which in experiments are modelled by a transition between deep and shallow regions. The required extension of our model to the case of variable bottom topography is currently under way. This extension will ultimately allow us to explore a number of quantum analogue systems, including single-particle diffraction, corrals and tunnelling.

Acknowledgements

Appendix A. Stability analysis for the vibrating bath

We here present a short calculation that leads to an accurate prediction of the stability threshold and most unstable wavenumber for our parametrically driven flow. We shall find the approximate conditions for neutral stability of the subharmonic mode corresponding to $\omega_0/2$ in the undamped case. The main idea is to truncate the infinite Hill matrix for the modes arising from the Floquet analysis of the damped Mathieu equation (see Holmes 1995) restricted to neutrally stable modes. Consider the damped system of equations for the waves in Fourier space

$$\eta_t = k\phi - 2\nu k^2 \eta, \tag{A 1}$$

$$\phi_t = -g_\Gamma(t)\eta - \frac{\sigma}{\rho}k^2\eta - 2\nu k^2\phi, \tag{A 2}$$

where $g_\Gamma = g(1 + \Gamma \sin \omega_0 t)$. Proposing a solution of the following neutrally stable form

$$\eta \equiv N^+ e^{i\omega_0 t/2} e^{ikx} + N^- e^{-i\omega_0 t/2} e^{ikx}, \tag{A 3}$$

$$\phi \equiv M^+ e^{i\omega_0 t/2} e^{ikx} + M^- e^{-i\omega_0 t/2} e^{ikx}, \tag{A 4}$$

and substituting into the equations yields the truncated system

$$\frac{i\omega_0}{2}N^+ = kM^+ - 2\nu k^2 N^+, \tag{A 5}$$

$$\frac{i\omega_0}{2}M^+ = -gN^+ + \frac{ig\Gamma}{2}N^- + \frac{\sigma}{\rho}(-k^2 N^+) - 2\nu k^2 M^+, \tag{A 6}$$

$$-\frac{i\omega_0}{2}N^- = kM^- - 2\nu k^2 N^-, \tag{A 7}$$

$$-\frac{i\omega_0}{2}M^- = -gN^- - \frac{ig\Gamma}{2}N^+ + \frac{\sigma}{\rho}(-k^2 N^-) - 2\nu k^2 M^-. \tag{A 8}$$

Terms proportional to $e^{3i\omega_0 t/2}$ and higher harmonics have been neglected. However, as we shall see, this approximation is sufficient to obtain accurate predictions. A non-trivial solution $[N^+, M^+, N^-, M^-]^T$ will arise for non-zero determinant of the truncated

Hill matrix:

$$
\begin{vmatrix}
\left(\dfrac{i\omega_0}{2}+2\nu k^2\right) & -k & 0 & 0 \\[2mm]
g+\dfrac{\sigma}{\rho}k^2 & \left(\dfrac{i\omega_0}{2}+2\nu k^2\right) & -\dfrac{ig\Gamma}{2} & 0 \\[2mm]
0 & 0 & \left(-\dfrac{i\omega_0}{2}+2\nu k^2\right) & -k \\[2mm]
\dfrac{ig\Gamma}{2} & 0 & g+\dfrac{\sigma}{\rho}k^2 & \left(-\dfrac{i\omega_0}{2}+2\nu k^2\right)
\end{vmatrix}=0. \quad (A\,9)
$$

We note that the infinite block diagonal Hill matrix is obtained when all harmonics are included. Hence, neutrally stable oscillations must satisfy

$$
\left[\left(\frac{i\omega_0}{2}+2\nu k^2\right)^2+k\left(g+\frac{\sigma}{\rho}k^2\right)\right]\left[\left(\frac{-i\omega_0}{2}+2\nu k^2\right)^2+k\left(g+\frac{\sigma}{\rho}k^2\right)\right]-\frac{g^2\Gamma^2}{4}k^2=0,
$$
$$(A\,10)$$

which simplifies to the expression (2.35) in the text. If we fix ω_0, this gives Γ as a function of k, the neutral curve in the Γ–k plane as shown in figure 1.

Below the minimum at (k_*, Γ_F) shown in figure 1, one can estimate the temporal decay rate of the Faraday modes, specifically $s < 0$ in a uniform decay of the form e^{st}. This can be found by replacing $2\nu k^2$ by $2\nu k^2 + s$ in (A 10) and making a suitable approximation for s near (k_*, Γ_F). For small s, the result is

$$
s=\frac{g^2\Gamma_F\delta\Gamma}{16\nu[\omega^2(k_*)+(2\nu k_*^2)^2+\frac{1}{4}\omega_0^2]}, \quad (A\,11)
$$

where $\delta\Gamma = \Gamma - \Gamma_F$. One may express this decay rate in terms of a memory parameter, usually written $Me = 1/|s|T_F$, which is then given by

$$
Me=\frac{64\pi\nu[\omega^2(k_*)+(2\nu k_*^2)^2+\frac{1}{4}\omega_0^2]}{\omega_0 g^2\Gamma_F^2}\left(1-\frac{\Gamma}{\Gamma_F}\right)^{-1}. \quad (A\,12)
$$

These formulae apply to the decay rate of a spatially extended standing wave (or of a Bessel function), but may not reflect the decay rate of more complex transient waves, such as those set up by a localized droplet impact.

Appendix B. Physical parameters and constants used in the simulations

Physical parameters:

$$
\sigma = 20.6 \text{ dyn cm}^{-1} = 20.6 \times 10^{-3} \text{ kg s}^{-2}, \quad (B\,1)
$$
$$
\rho = 0.949 \text{ g cm}^{-3} = 949 \text{ kg m}^{-3}, \quad (B\,2)
$$
$$
\nu = \mu/\rho = 0.2 \text{ St} = 0.2 \text{ cm}^2 \text{ s}^{-1} = 2 \times 10^{-5} \text{ m}^2 \text{ s}^{-1}, \quad (B\,3)
$$
$$
\mu_{air} = 1.8 \times 10^{-4} \text{ g cm}^{-1} \text{ s}^{-1} = 1.8 \times 10^{-5} \text{ kg m}^{-1} \text{ s}^{-1}, \quad (B\,4)
$$
$$
g = 980 \text{ cm s}^{-2} = 9.8 \text{ m s}^{-2}, \quad (B\,5)
$$
$$
\omega_0 = 80 \times 2\pi \text{ s}^{-1}. \quad (B\,6)
$$

The system parameters used for the single-drop simulations were

$$c_1 = 0.7, \quad c_2 = 8, \quad c_3 = 0.7, \quad c_4 = 0.13. \tag{B 7a−d}$$

For the numerical experiments involving two drops, it was only possible to observe the more complex patterns of interactions (i.e. orbiters and promenaders) by using higher values of c_4 (i.e. $c_4 = 0.3$, $c_4 = 0.32$).

REFERENCES

AMBROSE, D. M., BONA, J. L. & NICHOLLS, D. P. 2012 Well-posedness for water waves with viscosity. *J. Discrete Continuous Dyn. Syst.* B **17**, 1113–1137.

BACCHIAGALUPPI, G. & VALENTINI, A. 2009 *Quantum Theory at the Crossroads: Reconsidering the 1927 Solvay Conference*. Cambridge University Press.

BACH, R., POPE, D., LIOU, S. & BATELAAN, H. 2013 Controlled double-slit electron diffraction. *New J. Phys.* **15**, 033018.

BENJAMIN, T. B. & URSELL, F. 1954 The stability of the plane free surface of a liquid in vertical periodic motion. *Proc. R. Soc. Lond.* A **225**, 505–515.

BORGHESI, C., MOUKHTAR, J., LABOUSSE, M., EDDI, A., FORT, E. & COUDER, Y. 2014 The interaction of two walkers: wave-mediated energy and force. *Phys. Rev.* E **90**, 063017.

DE BROGLIE, L. 1926 *Ondes et mouvements*. Gauthier-Villars.

DE BROGLIE, L. 1930 *An Introduction to the Study of Wave Mechanics*. Methuen.

DE BROGLIE, L. 1956 *Une interprétation causale et non linéaire de la Mécanique ondulatoire: la théorie de la double solution*. Gauthier-Villars.

DE BROGLIE, L. 1987 Interpretation of quantum mechanics by the double solution theory. *Ann. Fond. Louis de Broglie* **12**, 1–23.

BUSH, J. W. M. 2010 Quantum mechanics writ large. *Proc. Natl Acad. Sci. USA* **107**, 17455–17456.

BUSH, J. W. M. 2015 Pilot-wave hydrodynamics. *Annu. Rev. Fluid Mech.* **47**, 269–292.

COUDER, Y. & FORT, E. 2006 Single particle diffraction and interference at a macroscopic scale. *Phys. Rev. Lett.* **97**, 154101.

COUDER, Y., FORT, E., GAUTIER, C.-H. & BOUDAOUD, A. 2005a From bouncing to floating: noncoalescence of drops on a fluid bath. *Phys. Rev. Lett.* **94**, 177801.

COUDER, Y., PROTIÈRE, S., FORT, E. & BOUDAOUD, A. 2005b Walking and orbiting droplets. *Nature* **437**, 208.

CROMMIE, M. F., LUTZ, C. P. & EIGLER, D. M. 1993a Imaging standing waves in a two-dimensional electron gas. *Nature* **363**, 524–527.

CROMMIE, M. F., LUTZ, C. P. & EIGLER, D. M. 1993b Confinement of electrons to quantum corrals on a metal surface. *Science* **262**, 218–220.

DIAS, F., DYACHENKO, A. I. & ZAKHAROV, V. E. 2008 Theory of weakly damped free-surface flows: A new formulation based on potential flow solutions. *Phys. Lett.* A **372**, 1297–1302.

EDDI, A., DECELLE, A., FORT, E. & COUDER, Y. 2009a Archimedean lattices in the bound states of wave interacting particles. *Europhys. Lett.* **87**, 56002.

EDDI, A., FORT, E., MOISY, F. & COUDER, Y. 2009b Unpredictable tunneling of a classical wave-particle association. *Phys. Rev. Lett.* **102**, 240401.

EDDI, A., MOUKHTAR, J., PERRARD, J., FORT, E. & COUDER, Y. 2012 Level splitting at a macroscopic scale. *Phys. Rev. Lett.* **108**, 264503.

EDDI, A., SULTAN, E., MOUKHTAR, J., FORT, E., ROSSI, M. & COUDER, Y. 2011 Information stored in Faraday waves: the origin of a path memory. *J. Fluid Mech.* **674**, 433–463.

EDDI, A., TERWAGNE, D., FORT, E. & COUDER, Y. 2008 Wave propelled ratchets and drifting rafts. *Europhys. Lett.* **82**, 44001.

FORT, E., EDDI, A., BOUDAOUD, A., MOUKHTAR, J. & COUDER, Y. 2010 Path memory induced quantization of classical orbits. *Proc. Natl Acad. Sci. USA* **107**, 17515–17520.

GILET, T. & BUSH, J. W. M. 2009a The fluid trampoline: droplets bouncing on a soap film. *J. Fluid Mech.* **625**, 167–203.

GILET, T. & BUSH, J. W. M. 2009*b* Chaotic bouncing of a droplet on a soap film. *Phys. Rev. Lett.* **102**, 014501.

HARRIS, D. M. & BUSH, J. W. M. 2014 Droplets walking in a rotating frame: from quantized orbits to multimodal statistics. *J. Fluid Mech.* **739**, 444–464.

HARRIS, D. M., MOUKHTAR, J., FORT, E., COUDER, Y. & BUSH, J. W. M. 2013 Wavelike statistics from pilot-wave dynamics in a circular corral. *Phys. Rev.* E **88**, 011001,1–5.

HOLMES, M. H. 1995 *Introduction to Perturbation Methods*, Texts in Applied Mathematics, vol. 20. Springer.

KUMAR, K. 1996 Linear theory of Faraday instability in viscous liquids. *Proc. R. Soc. Lond.* A **452**, 1113–1126.

KUMAR, K. & TUCKERMAN, L. S. 1994 Parametric instability of the interface between two fluids. *J. Fluid Mech.* **279**, 49–68.

LABOUSSE, M., PERRARD, S., COUDER, Y. & FORT, E. 2014 Build-up of macroscopic eigenstates in a memory-based constrained system. *New. J. Phys.* **16**, 113027.

LAMB, H. 1932 *Hydrodynamics*. Cambridge University Press.

MILEWSKI, P. A. & TABAK, E. G. 1999 A pseudospectral procedure for the solution of nonlinear wave equations with examples from free-surface flows. *SIAM J. Sci. Comput.* **21** (3), 1102–1114.

MOLÁČEK, J. & BUSH, J. W. M. 2012 A quasi-static model of drop impact. *Phys. Fluids* **24**, 127103.

MOLÁČEK, J. & BUSH, J. W. M. 2013*a* Drops bouncing on a vibrating bath. *J. Fluid Mech.* **727**, 582–611.

MOLÁČEK, J. & BUSH, J. W. M. 2013*b* Drops walking on a vibrating bath: towards a hydrodynamic pilot-wave theory. *J. Fluid Mech.* **727**, 612–647.

OZA, A. U., HARRIS, D. M., ROSALES, R. R. & BUSH, J. W. M. 2014*a* Pilot-wave dynamics in a rotating frame: on the emergence of orbital quantization. *J. Fluid Mech.* **744**, 404–429.

OZA, A. U., HARRIS, D. M., ROSALES, R. R. & BUSH, J. W. M. 2014*b* Pilot-wave dynamics in a rotating frame: exotic orbits. *Phys. Fluids* **26**, 082101.

OZA, A. U., ROSALES, R. R. & BUSH, J. W. M. 2013 A trajectory equation for walking droplets: hydrodynamic pilot-wave theory. *J. Fluid Mech.* **737**, 552–570.

PERRARD, S., LABOUSSE, M., MISKIN, M., FORT, E. & COUDER, Y. 2014 Self-organization into quantized eigenstates of a classical wave-driven particle. *Nature Commun.* **5**, 3219.

PROTIÈRE, S., BOHN, S. & COUDER, Y. 2008 Exotic orbits of two interacting wave sources. *Phys. Rev.* E **78**, 36204.

PROTIÈRE, S., BOUDAOUD, A. & COUDER, Y. 2006 Particle-wave association on a fluid interface. *J. Fluid Mech.* **554**, 85–108.

PROTIÈRE, S., COUDER, Y., FORT, E. & BOUDAOUD, A. 2005 The self-organization of capillary wave sources. *J. Phys.: Condens. Matter* **17**, 3529–3535.

WALKER, J. 1978 Drops of liquid can be made to float on the liquid. What enables them to do so? *Sci. Am.* **238**, 151–158.

WANG, Z. & MILEWSKI, P. A. 2012 Dynamics of gravity–capillary solitary waves in deep water. *J. Fluid Mech.* **708**, 480–501.

WIND-WILLASSEN, O., MOLÁČEK, J., HARRIS, D. M. & BUSH, J. W. M. 2013 Exotic states of bouncing and walking droplets. *Phys. Fluids* **25**, 082002.